

The effect of simulated hypervelocity space debris on polymers

R. Verker^{a,b,*}, N. Eliaz^b, I. Gouzman^a, S. Eliezer^c, M. Fraenkel^c, S. Maman^c,
F. Beckmann^d, K. Pranzas^d, E. Grossman^a

^a Space Environment Division, Soreq NRC, Yavne 81800, Israel

^b Department of Solid Mechanics, Materials and Systems, Tel Aviv University, Ramat Aviv, Tel Aviv 69978, Israel

^c Department of Plasma Physics, Soreq NRC, Yavne 81800, Israel

^d Department of Neutron Scattering, GKSS, Geesthacht 21502, Germany

Received 31 May 2004; received in revised form 8 August 2004; accepted 13 August 2004

Available online 15 September 2004

Abstract

Space debris population in low Earth orbit has been increasing constantly with the increase in spacecraft missions. Hypervelocity space debris impacts limit the functionality of polymeric outer surfaces and, in extreme cases, might cause a total loss of a spacecraft. In this work, the fracture of Kapton films by ultrahigh velocity impacts was studied. A laser-driven flyer ground simulation system was used to accelerate aluminum flyers to impact velocities as high as 2.9 km/s against polymer films with different thicknesses. Scanning electron microscopy was used to characterize the fracture morphology. Impact effects on the internal structure of the polymer were studied by means of X-ray microtomography. It was found that with an increase in debris velocity, a ductile-to-brittle transition occurred. However, fractures created by impacts at velocities above 1.7 km/s showed central impacts regions, which experienced the highest strain rate and were of ductile-type fracture, while the outer regions, which experienced a lower strain rate, failed through brittle cracking. A model explaining this phenomenon, based on the temperature gradient developed within the impacted region during collision, is presented.

© 2004 Acta Materialia Inc. Published by Elsevier Ltd. All rights reserved.

Keywords: Polymers; Fracture; Impact behavior; Scanning electron microscopy (SEM); Synchrotron radiation

1. Introduction

Most satellites nowadays are being launched into low Earth orbit (LEO) altitudes, ranging from 200 to 700 km. The LEO space environment possesses many obstacles to a successive spacecraft mission, either natural or man-made. The degrading environment for carbon-based materials, for example, includes atomic oxygen (AO), ultraviolet (UV) radiation, ionizing radiation (e.g., electrons and protons), ultrahigh vacuum (UHV), thermal cycles, micrometeoroids and orbital debris. Due to either singular or synergistic interactions

between these space components, structural materials – in particular polymer-based materials – suffer a relatively rapid erosion (mass loss), structure modification and surface roughening, leading to irreversible degradation of their optical, thermal, electrical and mechanical properties [1,2]. Therefore, a careful selection of satellite external surface materials, mainly polymer films and paints, is required [3].

Micrometeoroids originate naturally from planetary or asteroidal collisions and cometary ejecta [4]. Hypervelocity debris at LEO altitudes are man-made and consist mainly of large objects such as spent satellites and rockets, and mostly of small objects such as aluminum oxide fuel particles, paint chips and fragmentation objects from collisions of these bodies in orbit [4]. Typical velocities of debris particles range from few kilometers

* Corresponding author. Tel.: +972 8 943 4397; fax: +972 8 943 4403.

E-mail address: rverker@soreq.gov.il (R. Verker).

per second up to 16 km/s, making these particles a threat to spacecrafts. The debris issue must be quantified over the projected lifetime of a spacecraft to determine the life expectancy of exposed systems and to quantify necessary shielding requirements [5].

The recovery of several spacecrafts in the last decade has offered information concerning the directionality of the LEO meteoroids and space debris fluxes [6]. Such recovered spacecrafts and their parts include one of the Hubble space telescope solar arrays (retrieved at 1993), the European Retrievable Carrier – EURECA (retrieved at 1993), and the Long Duration Exposure Facility – LDEF (retrieved in 1990 after 69 months in LEO). Based on studies of the retrieved components or spacecrafts, the following conclusions have been drawn. Spacecraft debris impacts can degrade the performance of exposed spacecraft materials and, in some cases, prevent the satellite from performing or completing its mission [3]. The Hubble's solar array, for example, suffered impacts at ultrahigh velocities ranging from 2.9 to 11.5 km/s from particles 7–98 μm in diameter [7]. Particles traveling at ultrahigh velocities generated temperatures of approximately 4700 $^{\circ}\text{C}$ and pressures of several mega-Bars when they collided with a surface [8]. Accumulation of impacts over the large surface area of solar panels has led, in some cases, to degradation in efficiency [9].

Impacts into metals form craters, which have diameters averaging about five times the impact diameter. These craters are of concern because they can prevent impacted components from operating. In the case of composites, if a complete penetration occurs, it can lead to further breakdown of the composite during subsequent exposure to AO or VUV. Debris impacts into polymer films occur quite often, since they are used extensively onboard spacecrafts, mainly as thermal blankets. Mostly, these materials are thin laminated layers; thus the impacts cause delamination of these layers into many times the diameter of the crater [3]. Thermal control materials on the LDEF have demonstrated the significant synergism of orbital debris with other space environment. These synergisms further expanded the damaged areas caused by impacts. For example, the top surface of a metalized Mylar sample aboard the LDEF was completely eroded, exposing the interior surfaces to VUV radiation, AO and thermal cycling.

As the number of missions sent into LEO is increasing, the frequency of debris impacts is expected to increase as well [3]. Such an increase may lead to further complications in operation of satellites in LEO environment. These complications may be in the form of (i) accelerated development of molecular and particle contamination, and (ii) an increased change in optical and mechanical properties due to debris impact. Thermal blankets that cover large parts of a spacecraft will particularly be subjected to these changes. The expected

increase in impact frequency, in combination with the common use of polymeric thermal blankets onboard spacecrafts, provides the main motivation of this study. In this work, the fracture of Kapton films (the most common polymer in space applications) by hypervelocity impacts was studied. Following description of the experimental procedures in Section 2, the results and discussion will be provided in Section 3.

2. Experimental procedures

In this section, we first describe in Section 2.1 the laser driven flyer (LDF) method that was applied at Soreq NRC. In Section 2.2, a complementary technique that was developed especially to measure the flyer velocity in situ and in real time is presented. Finally, Section 2.3 describes the materials and characterization techniques that were used.

2.1. The laser-driven flyer ground simulation method

For the simulation of spacecraft hypervelocity debris with dimensions ranging from 10 to 100's μm and impact velocities of up to 3 km/s, the LDF method was used. LDF is attractive as an acceleration technique for debris simulation due to its relative simplicity, low cost, ease of incorporation into a vacuum facility, and high shot rate capability [8,10,11].

Fig. 1 shows a schematic diagram of the LDF process. The heart of Soreq's LDF system is a high-power Sapphire: Titanium laser (Thompson, Inc.) with two optional pulse lengths: 50 fs and 300 ps, the latter being used in this work. The wavelength in which the laser operates is 810 nm, and a range of pulse energies is available – from 250 to 750 mJ. The laser beam is guided through a set of mirrors into a vacuum chamber operating at a base pressure of 20 mTorr (Fig. 1b). Before entering the chamber, the beam passes through a focusing lens attached to a linear motion mechanism. Inside the chamber (Fig. 1a), the laser beam irradiates a 12 μm -thick pure aluminum foil through a BK7 glass substrate, to which it is tenaciously bonded (this laminate being referred, hereafter, as target). The beam passes through the glass without interacting with it, until it hits the aluminum/glass interface. At the interface, a high-temperature and high-pressure plasma is formed, which then expands perpendicularly to the foil. The theory of laser-plasma interaction, which is responsible in this work to the production of the projectiles, is explained in detail elsewhere [12]. Briefly, the expanding plasma induces a shock wave in the target, moving faster than the speed of sound toward the free (rear) surface. When the shock wave reaches the free surface, the latter is accelerated, and the former is reflected as a rarefaction wave. The rarefaction wave, moving in an opposite

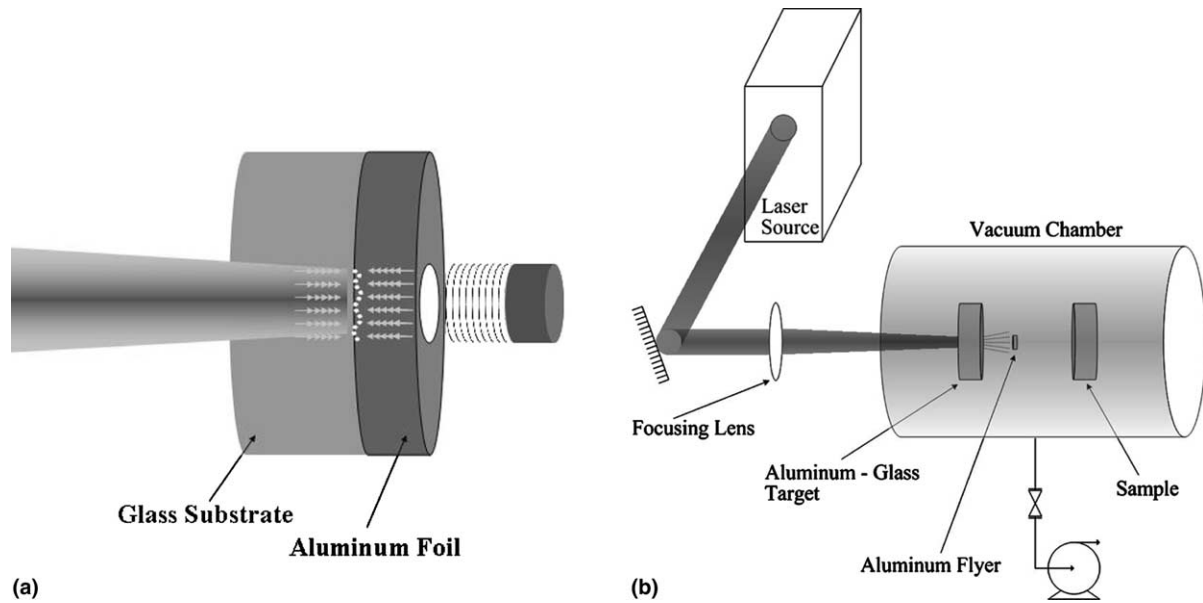


Fig. 1. (a) Schematic description of the LDF process, and (b) the experimental setup used in this work.

direction, causes deceleration of the free surface. The two rarefaction waves (i.e., the tail of the initial pressure wave and the wave reflected from the free surface), running in opposite directions, generate tension of the material. When the tension (i.e., negative pressure) exceeds the material spall pressure, a spall forms in a plane parallel to the rear surface. The spall may be defined as the process of internal failure or rupture of the media due to stresses in excess of the tensile strength of the material. A pressure gradient between the plasma pressure on one side and the vacuum zero pressure on the other side causes the spalled layer acceleration, which results in an aluminum layer to fly away at ultrahigh velocity as high as about 3 km/s. The size of the aluminum flyer formed is of the order of the beam spot size hitting the surface. By changing the distance of the focusing lens from the target, the spot size can be controlled, thus controlling also the flyer velocity. The aluminum flyers in this work were accelerated towards polymer samples, which were placed at a selectable distance of 2–12 mm from the target.

The selection of a suitable process for the fabrication of the metal/glass laminates is crucial for the success of the LDF method. A tenacious bond is required to achieve the desired velocities. The bond must allow the highest possible pressure to be attained, and the “break loose” stress should be a function of the metal yield strength rather than the interface bond strength [11]. In this project, the method used for production of proper metal/glass bonding is the field-assisted diffusion bond method. After cleaning both the glass substrate and the aluminum foil, they are placed between two heavy metal rods, which serve as the anode and cathode. This structure is then placed vertically inside a furnace and connected to a

high-voltage power supply. The system is heated to 370 °C, and a voltage of 300 V is applied for 10 s. Subsequently, the system is cooled to room temperature.

2.2. Flyer velocities measurement

The flyer velocity is a function of the laser beam spot size (as described in Section 2.1) and pulse energy. The theoretical flyer velocity is the maximum possible velocity obtained when assuming a system’s hydrodynamic efficiency, $\eta_h = 1.0$. This value means that the whole laser pulse energy is transformed into flyer kinetic energy. The hydrodynamic efficiency is defined as:

$$\eta_h = E_{kf}/E_{lp} = v_m^2/v_t^2, \quad (1)$$

where E_{kf} is the flyer kinetic energy, E_{lp} is the laser pulse energy, v_m and v_t are the measured and theoretical velocities, respectively.

In this work, a very simple setup was designed and put together in order to measure the flyer velocity in situ. This setup is shown schematically in Fig. 2(a). A continuous He:Ne laser beam is set orthogonal to the flyer’s trajectory, and by using a prism the beam crosses the flyer path twice. The two parallel beams are set at a known distance of 13 mm from each other. A photodiode attached to a scope receives the continuous laser signal. As the flyers cross the continuous laser’s path, two peaks are detected by the scope, allowing the velocity calculation. Fig. 2(b) shows a typical scope display for a laser pulse energy of 650 mJ, with two intensity peaks evident approximately 6 μ s apart, corresponding to a flyer velocity of 2 km/s. One should note that the broad peak results from the formation of many projectiles, rather than just one effective projectile.

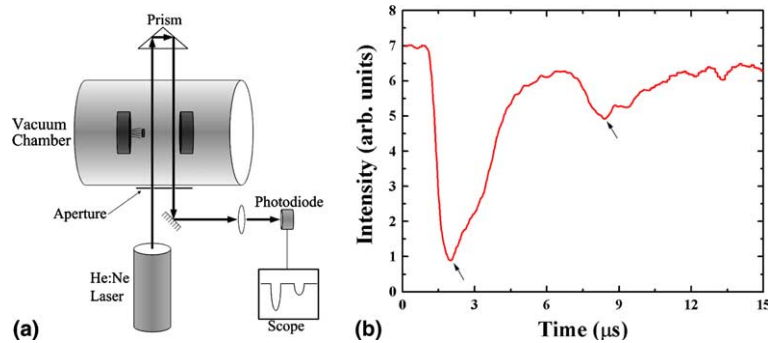


Fig. 2. (a) Schematic description of the flyer velocity measurement setup, and (b) a typical scope display for an LDF experiment with a laser pulse energy of 650 mJ, revealing two peaks (marked by arrows) approximately 6 μs apart.

2.3. Materials and characterization techniques

The material studied in this work is commercial Kapton HN Polyimide (DuPont, Inc.) in the form of 25, 50 and 125 μm -thick films. The selection of this material is not arbitrary. Kapton possesses a unique combination of properties that makes it attractive for a variety of applications onboard of spacecrafts. Its main use is as the outer layer of multilayer thermal control insulation blankets, and also as flexible substrates for high-power solar arrays. Among its main properties are: inherent strength, temperature stability, excellent insulation properties, and stability under ionizing and UV radiation. Kapton is also known for its superior optical properties, including low solar absorbance and high thermal emittance.

The morphology of craters and fractures resulting from the debris impacts is studied using an environmental scanning electron microscope (ESEM, model Quanta 200 from FEI). This microscope allows characterization of degassing and non-conductive samples (e.g., Kapton and glass) without the need for a conductive coating.

Impact effects on the internal three-dimensional microstructure of Kapton are studied by means of the direct, non-invasive X-ray absorption micro-computerized tomography ($\mu\text{-CT}$) [13]. This technique is the extension of CT; it creates cross-sectional images with a spatial resolution approaching 1 μm . Obtaining a high spatial resolution requires X-ray sources with a high photon flux. For this purpose, the use of synchrotron radiation is particularly attractive because it allows for high photographic resolution on the micrometer scale. Synchrotron radiation has numerous potential applications in various fields, mainly for the investigation of materials (e.g., alloys, porous media, or composite materials), but also for biological or geological samples. Perhaps most important, the tunability of a synchrotron source can be used to create tomographic images above and below the absorption edge of many elements, and provides the ability to make three-dimensional concentration mapping of those elements. Synchrotron radia-

tion-based $\mu\text{-CT}$ is performed in this project at beamline BW2 of HASYLAB at DESY (Hamburg, Germany), using monochromatic X-rays [14].

3. Results and discussion

In Section 3.1 we first characterize the flyers in LDF experiments in terms of their sizes and velocities. Next, in Section 3.2 we present $\mu\text{-CT}$ data that helps in evaluation of the microstructural damage that results from impacting the Kapton foils. Section 3.3 then presents SEM analysis of the craters and cracking associated with debris impacts under different conditions of polymer foil thickness and flyer velocity. Finally, in Section 3.4 the authors suggest a model to explain the different fracture modes observed, in terms of an energy balance and the related temperature gradient that forms in the material when impacted.

3.1. Measurements of flyer velocity and flyer size

As described in Section 2.2, the flyer velocity is a function of the laser beam spot size and pulse energy. Fig. 3 shows the theoretical (i.e., kinetic energy definition) and measured flyer velocities as a function of the laser's pulse energy. The ordinate error bars in this figure were drawn based on the minimal and maximal deviation between the two scope peaks at full width at half maximum (FWHM). It is noted that at the highest pulse energy attainable (750 mJ), a flyer velocity of 2.9 km/s is measured. When applying the theoretical and measured velocities into Eq. (1), the Soreq's LDF system hydrodynamic efficiency may be calculated as $\eta_h = 0.23$.

In order to estimate the flyer size, a series of four experiments was conducted, using a 1.6 mm-thick BK7 glass as the impacted sample. All experiments were carried out using similar parameters: pulse energy 250 mJ, vacuum pressure 100 mTorr, pulse duration 300 ps, and a flyer velocity of 1.4 km/s. Fig. 4 shows a typical ESEM

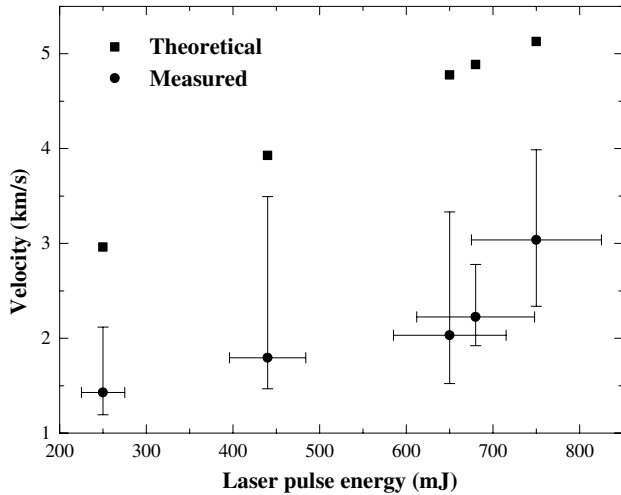


Fig. 3. The flyer measured and theoretical velocities as a function of the laser pulse energy.

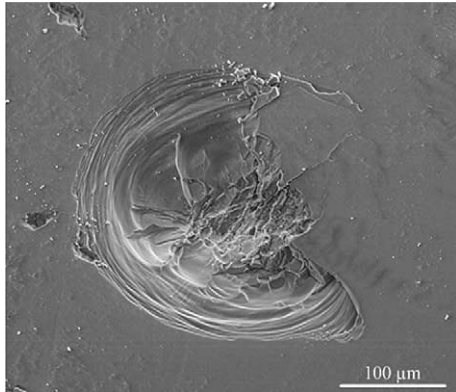


Fig. 4. A typical ESEM image of an impact-induced crater on a glass surface. Impact conditions are: 250 mJ pulse energy, 300 ps pulse duration, 100 mTorr base pressure, and 1.4 km/s flyer velocity.

image of an impact-induced crater on the glass surface. The flyer effective diameter, d_f , can be calculated using the ‘Conchoidal Cracking Diameter Equation’ [7]:

$$d_{co} = 5 \times 10^{-4} \rho_s^{-0.5} \rho_f^{0.71} d_f^{1.13} v_f^{0.754}, \quad (2)$$

where d_{co} is the diameter of the outer concentric cracking region (measured on Fig. 4), ρ_s and ρ_f are the sample (glass) and flyer (aluminum) densities, respectively, and v_f is the flyer velocity (measured as in Fig. 3). The values are substituted into Eq. (2) in cgs units. This calculation yielded an effective flyer diameter within the range of 23–29 μm for all experiments. This repeatability of results seems to be very good. It should be noted, however, that each laser shot at the target produces in practice a cloud of flyers with different diameters, all traveling at ultrahigh velocities. The existence of such a cloud is evident by the width and asymmetry of the peaks in Fig. 2(b) and by the microtomography results (see Section 3.2).

3.2. Microtomography analysis of the internal impact-induced damage

As described in Section 2.3, impact effects on the internal three-dimensional microstructure of Kapton are studied by means of microtomography ($\mu\text{-CT}$). This technique provides three-dimensional representations of a specimen by reconstructing a series of two-dimensional absorption images. Here, preliminary data from a comprehensive work is presented. Fig. 5 shows two-dimensional cuts through a three-dimensional image of a 125 μm -thick Kapton sample impacted by 2.9 km/s debris. Fig. 5(a) shows a top-view cut of the impacted Kapton just below the surface. The white regions are aluminum particles imbedded in the polymer at the displayed depth. The dark areas are holes created by the impacts. These results provide information on the size and distribution of the debris. It is evident that the cloud of aluminum flyers created by the LDF system is composed of several small debris, each of the order of few tens of micrometers in size. This observation supports the results presented in Section 3.1. Fig. 5(b) shows a cross-section of the impacted sample, revealing – besides of the observed holes – also the formation of longitudinal cracks. These cracks originate from debris impacts and the related spallation process. The spallation process has already been explained in Section 2.1. In brief, when the tension amplitude generated by the two rarefaction waves exceeds the tensile strength of Kapton, a dynamic fracture (i.e., spall) occurs – see Fig. 6. The engineering fracture strain, ϵ_f , due to shock wave effects only, may be defined based on the general relation [15]

$$\epsilon_f = (L_f - L_0)/L_0, \quad (3)$$

where L_0 is the initial sample length and L_f is its length at fracture. This equation is obviously only an approximation when carrying out the measurement of L_f ex situ, after the fracture already occurred, because it ignores the elastic strain that is released upon fracture. Yet, it is satisfactory for the following estimation of strain rate. From Eq. (3) and measurement of L_f on Fig. 6, $\epsilon_f = 14.2\%$ is obtained. Assuming that all waves propagate inside the material at the speed of sound (1326 m/s is considered herein [16,17]), the time required for them to propagate to failure is approximately $t_f = 1.4 \times 10^{-7}$ s. Hence, the strain rate that Kapton experienced during the dynamic process is ultrahigh – approximately 1.0×10^6 1/s.

3.3. The effects of polymer film thickness and flyer velocity on cratering and cracking appearance

In this section, typical ESEM images are shown and used to characterize the morphology of cracking in impacted samples, for different thicknesses and flyer velocities.

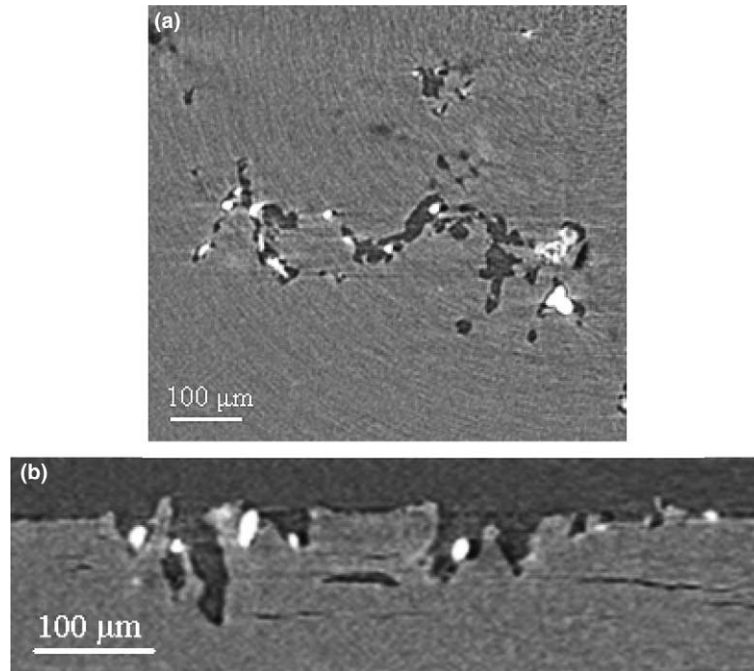


Fig. 5. X-ray microtomography two-dimensional cuts through a three-dimensional image of 125 μm -thick Kapton sample impacted by 2.9 km/s debris. (a) Shows a top-view just below the surface, while (b) shows the cross-section.

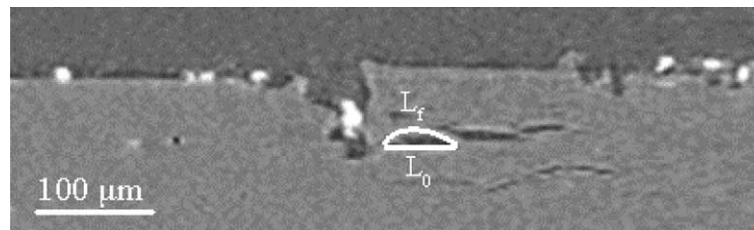


Fig. 6. A cross-section of X-ray microtomography from a 125 μm -thick Kapton impacted by 2.9 km/s debris. A spall created by the impact is evident and used to estimate the fracture strain.

The effect of film thickness on the extent and nature of damage introduced into the Kapton film is demonstrated in Fig. 7. Laser driven flyers with velocity of 1.73 km/s are shot in this case against 25, 50 and 125 μm -thick Kapton films. All images in Fig. 7 are acquired from the impacted sample exit side. It is evident that as the film thickness increases, a transition from brittle (Fig. 7(a)) to ductile (Fig. 7(c)) fracture occurs, and the overall extent of damage caused by the impact is reduced too (note the different scale bar). The 25 μm -thick Kapton film (Fig. 7(a)) has experienced significant damage with radial brittle-like cracks emanating from a central impact zone. The 50 μm -thick Kapton film (Fig. 7(b)) experienced less damage, lacking any radial cracks; only few punctures are noticed. The least damage is introduced into the 125 μm -thick Kapton film (Fig. 7(c)); only a single penetration zone is observed, exhibiting a volcano-like puncture.

The following argument may be given to explain this thickness dependence behavior. As the Kapton film becomes thicker, its ability to absorb energy and slow

the flyer increases. Consequently, the strain rate associated with the impact process is reduced. For the 25 μm -thick film, the strain rate is high enough to catalyze the formation of brittle radial cracks. For the 50 μm -thick film, intermediate strain rates probably exist, leading to a semi-ductile fracture of the polymer. In this case, no sufficient energy is left to allow radial cracking. Finally, in the case of the 125 μm -thick film, only a single puncture is formed – most likely by a single flyer. The strain rate under which this process takes place is low enough to enable ductile fracture.

In order to support the suggested argument, a 50 μm -thick Kapton film was impacted at a velocity of 1.8 km/s and examined microscopically both from the impact side and the exit side. The aluminum flyer residues that are typically attached to the impact side were removed by rinsing the sample in a 15% hydrochloric acid for a period of 10 min. Microscopic examination (data not shown) of the exit side revealed a semi-ductile fracture, with almost clear shear of the polymer film and no crack

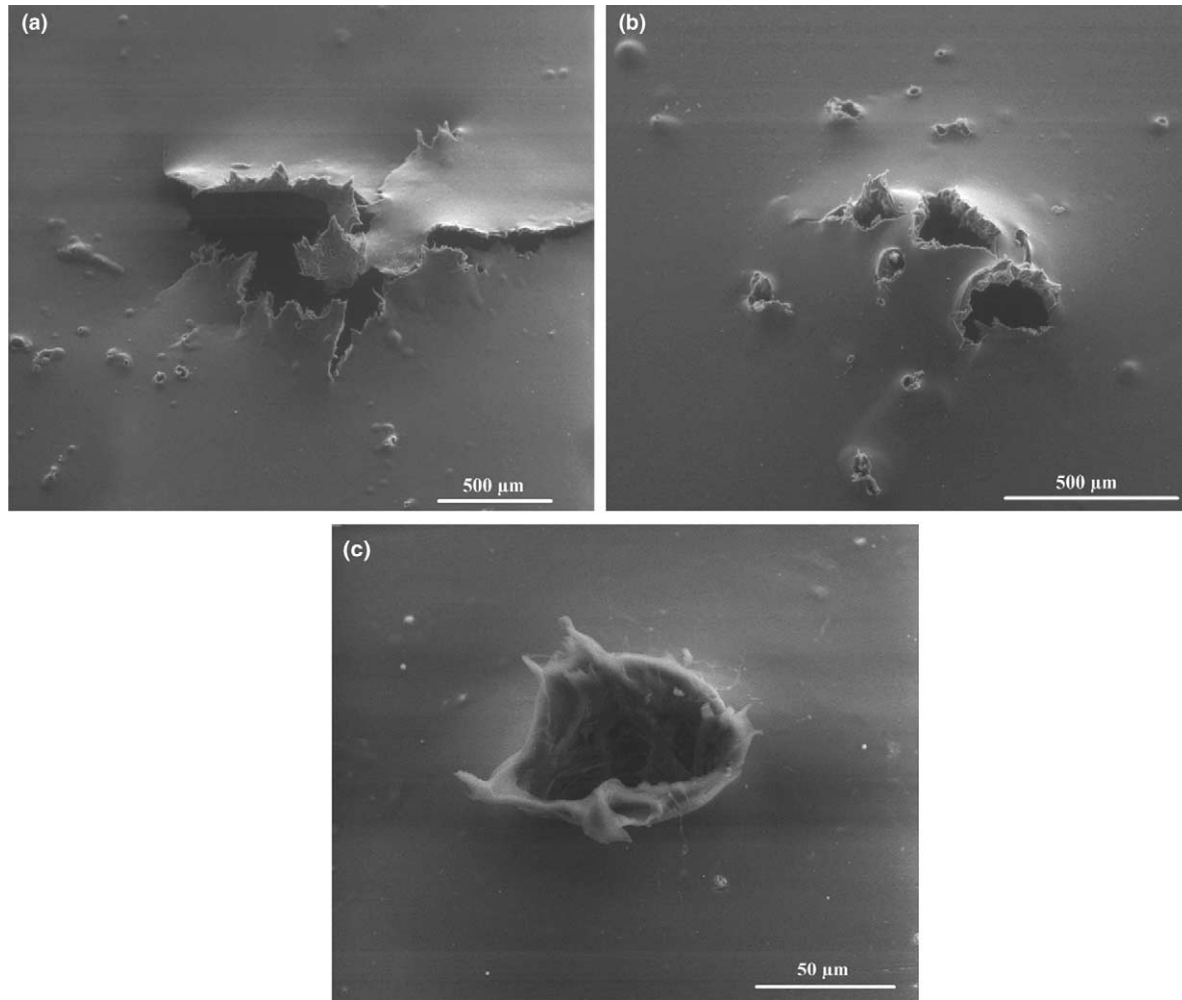


Fig. 7. Impacts at velocity of 1.7 km/s into: (a) 25 μm -, (b) 50 μm -, and (c) 125 μm -thick Kapton films. Note the different scale bar in (c).

formation. The impact side, on the other hand, exhibited a much more brittle nature, with shallow, surface radial cracks emanating from the same punctures observed from the exit surface. This more brittle shear-out fracture on the impact side as compared to the exit side, may bolster the argument of how thicker specimens slow down the projectile sufficiently to change fracture type.

Fig. 8 demonstrates the effect of flyer velocity on the extent and nature of damage developed in impacted 25 μm -thick Kapton films. The fractures are created using entrance flyer velocities v_f^i of 1.4 (Fig. 8(a)), 1.6 (Fig. 8(b)), 1.7 (Fig. 8(c)), and 2.9 (Fig. 8(d)) km/s. All ESEM images are taken from the exit side.

The volcano-like puncture sites obtained at the lowest velocity (Fig. 8(a)) may indicate ductile rupture of the polymer. At this relatively low velocity, only few flyers could penetrate the film and create the punctures. At a higher flyer velocity of 1.6 km/s (Fig. 8(b)), ductile rupture is still dominant, but some cracks begin to form around these volcano-like punctures. A further increase in the flyer velocity results in radial cracking around the

central impact zone (Fig. 8(c)). The results indicate also that all flyers in the cloud had sufficient energy to penetrate the Kapton film. At the highest tested velocity of 2.9 km/s, these radial cracks completely develop into a brittle fracture of the polymer (Fig. 8(d)). The transition from ductile to brittle fracture may be expected, because such transitions are strongly dependent on the strain rate. As the flyer velocity increases, the strain rate also increases. Brittle fractures are associated with less energy absorbance compared to ductile fractures [18].

At relatively low strain rates (Fig. 8(a) and (b)), the kinetic energy lost by the flyers is transferred into pronounced deformation energy. At relatively high strain rates (Fig. 8(c) and (d)), on the other hand, the successive kinetic energy is transformed into crack propagation energy and the associated formation of new surfaces.

A closer examination of the sample impacted at the highest velocity of 2.9 km/s (Fig. 8(d)) is given in Fig. 9. This figure shows also the fracture surface morphology (fractography) around the circumference of the penetrating hole. It is clear that this morphology

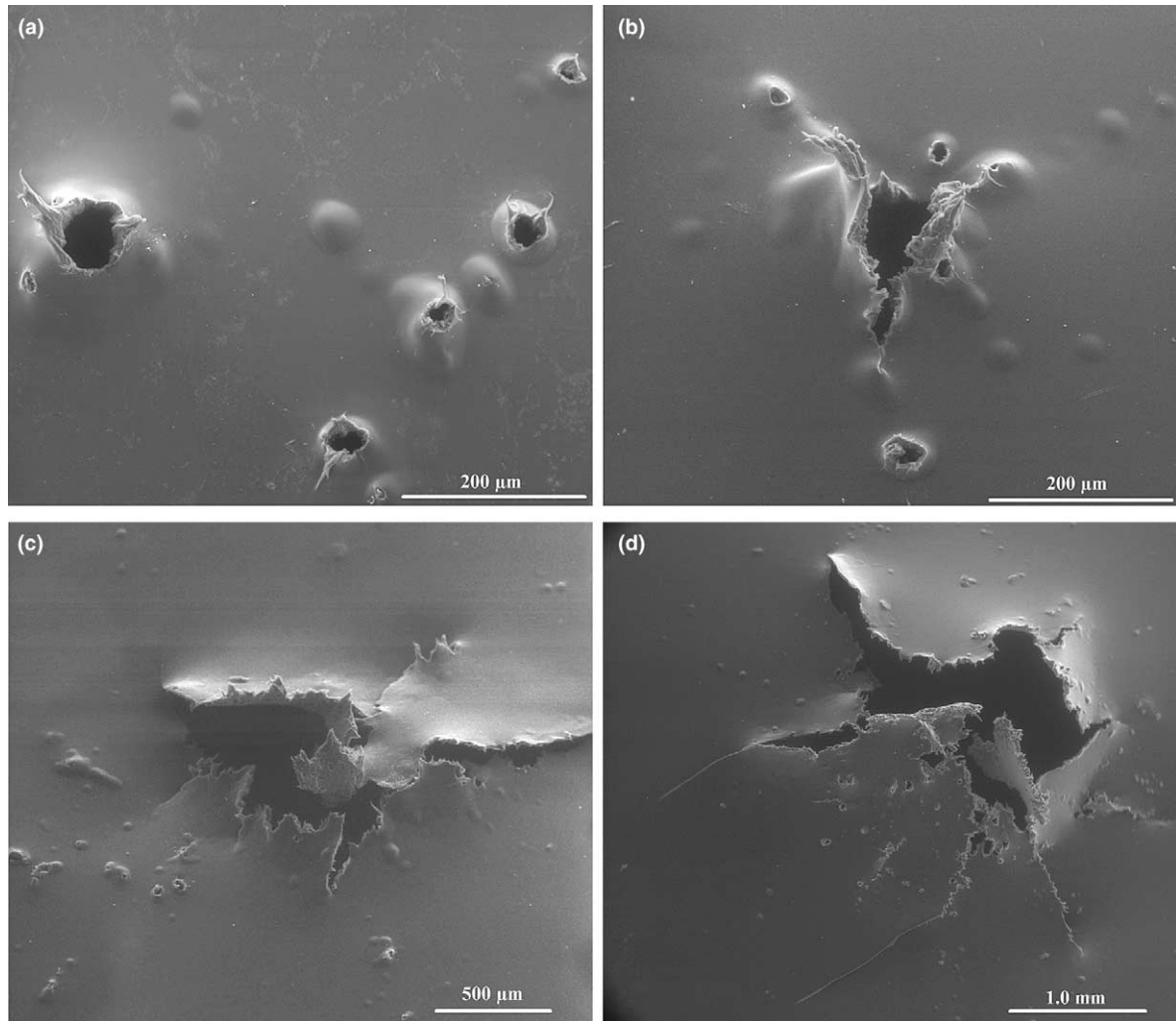


Fig. 8. ESEM images of 25 μm -thick Kapton films impacted by flyers at velocities of 1.4 km/s (a), 1.6 km/s (b), 1.7 km/s (c), and 2.9 km/s (d), respectively.

changes significantly, indicating the possible involvement of different modes of fracture. The characteristics of fracture morphology seem surprising at first – while the central penetration zone that experienced the highest strain rate fail in a fairly ductile manner, the radial cracks that formed subsequently under lower strain rates (i.e., as a secondary process) exhibit a more brittle fracture morphology. It is believed that this behavior can be explained in terms of a high temperature gradient that is established within the polymer sample as the flyer hits its surface and penetrates through the film. This is explained in the following section.

3.4. The temperature gradient model

In this section, a model is suggested to explain the different fracture modes observed (Fig. 9), in terms of an energy balance and the related temperature gradient that forms in the material when it is impacted. It is well known that ductile–brittle transitions depend strongly

on the local temperature. Whereas a ductile fracture is expected above the glass transition temperature, T_g , below this temperature brittle fractures are most likely to occur. It should be noted that in Kapton, a second-order transition occurs within the temperature range of 360–410 $^{\circ}\text{C}$, which is assumed to be the glass transition temperature [16]. This temperature dependence of fracture mode also reminds the deformation map suggested by Spaepen for metallic glasses [19]. Ultrahigh velocity impacts generate temperatures in the range of 1727–6727 $^{\circ}\text{C}$ and shock pressures of 30–100 GPa when striking ceramic surfaces [9,20]. High-density polyethylene projectiles shot at an average velocity of 5 km/s were observed to generate temperatures of up to 7927 $^{\circ}\text{C}$ in the case of head-on impacts on aluminum targets [21].

Hence, the following model can explain the phenomenon demonstrated in Fig. 9. Due to the high temperature generated at the penetration zone and despite the ultrahigh strain rate involved in the impact, the Kapton film exhibits a fairly ductile fracture in this zone (region

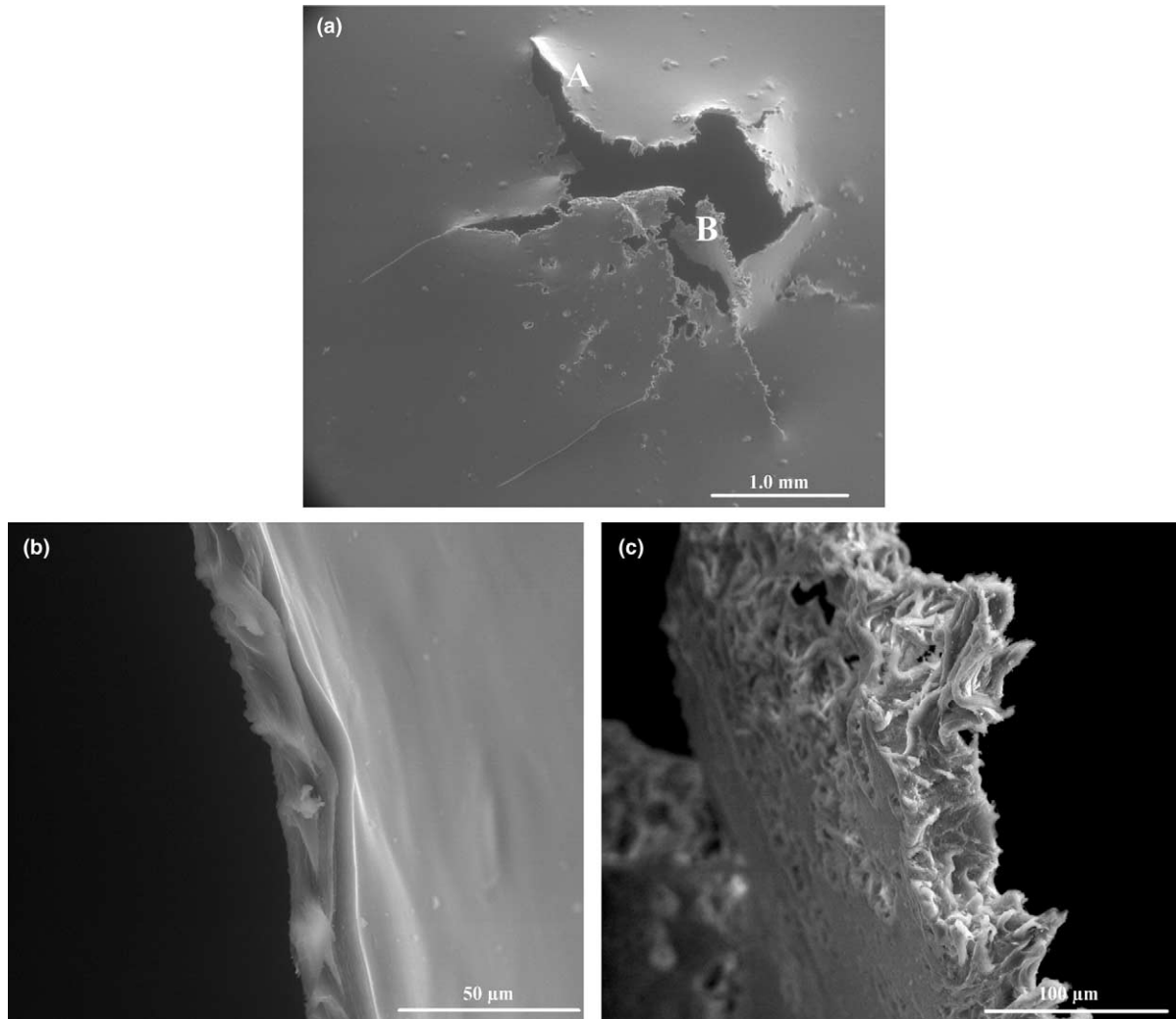


Fig. 9. (a) A 25 μm -thick Kapton film impacted at a hypervelocity of 2.9 km/s. Two distinct modes of fracture are evident: (b) a fairly brittle fracture in the radial cracking region (region A in (a)), and (c) a more ductile fracture around the central penetration region (region B in (a)).

B in Fig. 9a). On the other hand, the significantly lower temperatures of $T < T_g$ are not sufficient to compensate for the still high strain rates, thus the secondary cracks far from the impact point exhibit brittle–fracture characteristics (region A in Fig. 9a).

In order to support this model, one first has to estimate the mean temperature developed within a sample at the time of penetration. Fig. 10 shows a 25 μm -thick Kapton film impacted at an entrance flyer velocity v_f^i of 2.2 km/s. The flyer velocity at the exit, v_f^o , is also measured and found to be 1.54 km/s. The sample is divided into three distinct regions: (a) the penetration hole, at which a piece of Kapton was sheared-off, (b) a region where a ductile fracture is observed, and (c) a region where a brittle fracture is noticed. The system energy balance is expressed as follows:

$$\Delta E_{kf} = E_{ks} + E_{sh} + E_c + E_h, \quad (4)$$

where ΔE_{kf} is the loss of flyer kinetic energy due to impact, E_{ks} is the kinetic energy transferred to the piece of Kapton that was sheared-off, E_{sh} is the shearing energy, E_c is the energy required for crack propagation, and E_h is the energy transformed into heat, which results in temperature increase. It is assumed that no change in potential energy occurs.

The following assumptions are made in the calculation: (i) the impact is treated as an equilibrium process. Although this assumption is inaccurate, it greatly simplifies the calculation and provides the ability to calculate a mean temperature within a certain region of the sample; (ii) the velocity of the sheared Kapton piece is equal to the flyer velocity at the exit side, v_f^o ; and (iii) the energy required for deformation of the Kapton surface is relatively small, and may thus be neglected. ΔE_{kf} and E_{ks} are calculated according to the fundamental kinetic energy equation:

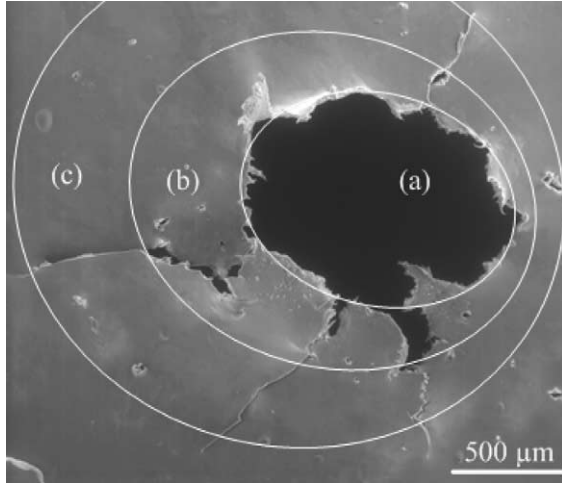


Fig. 10. A 25 μm -thick Kapton film impacted at a hypervelocity of 2.2 km/s. The sample is divided schematically into three regions: (a) the penetration hole, at which a piece of Kapton was sheared-off, (b) a region where a ductile fracture is observed, and (c) a region where a brittle fracture is noticed.

$$\Delta E_k = mv^2/2, \quad (5)$$

where m is either the flyer mass, m_f , or the mass of Kapton that was sheared-off (m_{sh}). E_{sh} is calculated according to:

$$E_{sh} = P_{sh}h/2, \quad (6a)$$

and

$$P_{sh} = 0.85hL\sigma_u, \quad (6b)$$

where P_{sh} is the shearing force, h is the film thickness, L is the length of cut, and σ_u is the ultimate tensile strength of the material being sheared. Eq. (6a) is an analytical

approximation that reflects the area under the force–displacement curve and includes a factor of 0.5 for a ductile material. Eq. (6b) includes a factor of 0.85, which also refers to a ductile material. Finally, E_c may be found from the general relation

$$E_c = 2h(\gamma_s + \gamma_p) \sum \delta a, \quad (7)$$

where γ_s is the specific surface energy, γ_p is the plastic deformation energy, and $\sum \delta a$ is the total length of cracks that formed by impact. Eq. (7) is the product of the total area of cracks formed and the specific energies associated with this cracking process. It takes into account that in polymers, as in metals, the fracture energy is much higher than the surface energy due to a large contribution from plastic deformation energy. This argument was considered in both Orowan's and Irwin's revisions to Griffith's crack theory. A summary of parameter values employed herein to solve Eqs. 5 through 7, is given in Table 1, together with the results of these calculations.

Now, by substituting these values into Eq. (4), the amount of energy transformed into heat may be estimated as $E_h = 30$ mJ. The common expression for heat capacity is adopted here [22]:

$$E_h = mc_p\Delta T, \quad (8)$$

where m is the mass of Kapton confined within region b in Fig. 10 ($m_g = 3.0 \times 10^{-5}$ gr), c_p is the specific heat of Kapton ($c_p = 1.09$ J/gr/K [16]), and ΔT is the temperature gradient. This expression assumes an adiabatic temperature rise (i.e., when no cooling occurs). Thus, a mean temperature increase $\Delta T = 920^\circ$ is found. This calculation shows that a flyer penetrating at a velocity of 2.2 km/s causes a significant temperature increase in

Table 1
Parameter values substituted into Eqs. 5 through 7 and the results of these energy balance calculations

Equation number	Parameter values employed	Source of value	Calculation result
5	$m_f = 5.7 \times 10^{-5}$ gr $v_f^i = 2.2$ km/s $v_f^o = 1.54$ km/s	Measured ^a Measured ^b Measured ^b	$\Delta E_{kf} = 70.2$ mJ
5	$m_{sh} = 3.4 \times 10^{-5}$ gr $v_f^o = 1.54$ km/s	Measured ^c Measured ^b	$E_{ks} = 40.0$ mJ
6b	$h = 25$ μm $L = 3.5$ mm $\sigma_u = 231$ MPa	Measured Measured ^d [16]	$P_{sh} = 17.2$ N
6a	$P_{sh} = 17.2$ N $h = 25$ μm	Calculated Measured	$E_{sh} = 0.2$ mJ
7	$\sum \delta a = 0.37$ cm $\gamma_s = 0.58$ mN/cm $\gamma_p = 0.5$ N/cm	Measured ^d [16] [23]	$E_c = 9.3$ μJ

^a m_f was calculated as the product of aluminum flyer's area (sheared-off from the aluminum/glass laminate), the aluminum foil thickness (12 μm) and aluminum's density (2.7 g/cm³).

^b v_f^i and v_f^o were measured as described in Section 2.2.

^c m_{sh} was calculated as the product of region a area in Fig. 10, sample thickness and density.

^d L and $\sum \delta a$ were measured from Fig. 10.

the penetration zone (Fig. 10, region (b), raising the local average temperature to as high as approximately 947 °C. This estimated temperature is much higher than the glass transition temperature of Kapton, supporting the suggested model and explaining the ductile-like fracture within the penetration zone. This great temperature gradient also predicts a temperature lower than T_g in region c, where the high strain rate results in a brittle-like fracture.

4. Conclusions

A LDF system was built for simulation of space debris impacts. The system produces a cloud of flyers with diameters of up to 30 μm and measured velocities of 1.4–2.9 km/s. The effect of simulated hypervelocity debris impacts on space-qualified Kapton films is studied for different film thickness (25, 50 and 125 μm) and impact velocities.

As the Kapton film thickness is increased from 25 to 125 μm at a fixed impact velocity, a transition from brittle to ductile fracture is observed. At a constant thickness of 25 μm , low impact velocities of 1.4–1.6 km/s result in a ductile-like fracture. Increasing the flyer velocity leads to cracking, mostly brittle-like. High-velocity impacts generate spalls in the Kapton film, with ultrahigh strain rate of about 10^6 s^{-1} . At impact velocities higher than 1.7 km/s, the central impact region, which is exposed to the highest strain rate, is characterized by a ductile-like fracture. Remote radial crack regions, on the other hand, are characterized by a brittle-like fracture in spite of the lower strain rates. A model explaining this phenomenon is suggested based on the high impact temperature ($T > T_g$) developed at the central impact region, and the low temperatures ($T < T_g$) at remote regions.

Acknowledgements

This work was partially supported by the Israeli Space Agency and by a grant from Geesthacht Neutron Facility (GeNF, Germany). The authors are grateful to Mr. Tilman Donath for his help in measurements at GKSS.

References

- [1] Grossman E, Gouzman I, Viel-Inguibert I, Diguirard M. *J Spacecraft Rockets* 2003;40:110.
- [2] Houdayer A, Cerny G, Klemberg-Sapieha JE, Czeremuskin G, Wertheimer MR. *Nucl Instrum Meth Phys Res B* 1997;131:335.
- [3] Silverman EM, *Space Environmental Effects on Spacecraft – LEO Material Selection Guide*, NASA Contractor Report No. 4661. Langley Research Center, 1995. p. 4-1.
- [4] Tennyson RC, Shortliffe G. In: Paillous A, editor. *Proceedings of the Seventh International Symposium on Materials in Space Environment* ESTEC Noordwijk, The Netherlands: ESA Publication; 1997. p. 485.
- [5] Hastings D, Garrett H. *Spacecraft–environment interactions* Cambridge, UK: Cambridge University Press; 1996. p. 45.
- [6] Miao J, Stark JPW. *Planet Space Sci* 2001;49:927.
- [7] Paul KG, Igenbergs EB, Berthoud L. *Int J Impact Eng* 1997;20:627.
- [8] Stein C, Roybal R, Tlomak P. In: Werling E, editor. *Proceedings of the Eighth International Symposium on Materials in Space Environment* Toulouse, France: CNES Publication; 2000.
- [9] Medina DF, Wright L, Campbell M. *Adv Space Res* 2001;28:1347.
- [10] Tighe A, Gabriel S, Van Eesbeek M. In: Werling E, editor. *Proceedings of the Eighth International Symposium on Materials in Space Environment* Toulouse, France: CNES Publication; 2000.
- [11] Roybal R, Tlomak P, Stein C, Stokes H. *Int J Impact Eng* 1999;23:811.
- [12] Eliezer S. *The interaction of high-power lasers with plasmas* Bristol: Institute of Physics; 2002.
- [13] Elmoutaouakkil A, Fuchs G, Bergounhon P, Péres R, Peyrin F. *J Phys D Appl Phys* 2003;36:A37.
- [14] Tadic D, Beckmann F, Schwarz K, Epple M. *Biomaterials* 2004;25:3335.
- [15] Gilath I, Eliezer S, Dariel MP, Kornblit L. *J Mater Sci Lett* 1988;7:915.
- [16] Du-Pont, Inc., Technical bulletin, <http://www.dupont.com/kapton/general/H-38492-2.pdf>.
- [17] Dillon RO, Abbas A, Lanno NJ, Ahmad A. *J Vac Sci Technol A* 2001;19:2826.
- [18] Callister WD. In: *Material science engineering* New York, USA: John Wiley & Sons, Inc.; 2000. p. 124.
- [19] Spaepen F. *Acta Metall* 1977;25:407.
- [20] Akins JA. *Dynamic Compression of Minerals in the MgO–FeO–SiO₂ System*, Ph.D. Thesis, California Institute of Technology, USA, 2003.
- [21] Ramjaun D, Shinohara M, Kato I, Takayama K. In: *Proceedings of the 23rd International Symposium on Shock Waves, ISSW23*, Fort Worth, Texas, USA, 22–27 July, 2001.
- [22] Smith JM, VanNess HC. *Introduction to chemical engineering thermodynamics* New York, USA: McGraw-Hill Book Company; 1975. p. 50.
- [23] Cenna AA, Allen S, Page NW, Dastoor P. *Wear* 2003;254:581.